LIQUID FLOW PAST NANOSCALE OBJECTS

BY

MARCUS HWAI YIK TAN

THESIS

Submitted in partial fulfillment of the requirements
for the degree of Master of Science in Theoretical and Applied Mechanics
in the Graduate College of the
University of Illinois at Urbana-Champaign, 2013

Urbana, Illinois

Adviser:

Professor Narayana R. Aluru

ABSTRACT

We present nonequilibrium molecular dynamics (MD) simulations of liquid flow past a carbon nanotube (CNT) and a single graphene sheet. We apply a gravity driven liquid argon flow past a CNT in a small domain and show that the drag coefficients can be modeled as Stokes flow past an array of CNT's with an effective diameter. The effective diameter can be obtained from the radial density profile around the CNT. We also apply a uniform flow of liquid argon and SPC/E water past a graphene sheet and show that the drag coefficient and the velocity profile can be modeled using Navier-Stokes equation provided corrections are applied to the equation. The corrections are the effective shape of the graphene sheet, the slip velocity correction and the viscosity and density layering correction. The effective shape can be obtained from the density profile plot around graphene. We use a separable solution of the elliptical cylindrical Stokes equation as a physical model to determine the slip velocity at the boundary of the effective shape by extrapolation. The viscosity and density layering correction is determined by calculating the local average density around the graphene sheet and using a viscosity equation of state. By applying these corrections, we show that good agreement between computational fluid dynamics (CFD) and MD can be obtained. Using a very large domain, agreement is also obtained between an analytical expression of the drag coefficient on an ellipse in an unbounded uniform flow derived by matched asymptotic expansion and MD for the case of strong interaction between argon and carbon atoms. Agreement is obtained for high Reynolds number for the weak interaction case as well.

To my parents, for their love and support.

ACKNOWLEDGMENTS

I would like to give special thanks to my advisor, Prof. Narayana R. Aluru for his support and guidance on my work towards the completion of this thesis.

I would also like to thank my fellow group-mates for helpful discussion.

I gratefully acknowledge the use of the parallel computing resource provided by the Computational Science and Engineering Program at the University of Illinois.

Last but not least, I am also grateful for the encouragement provided by my family members.

TABLE OF CONTENTS

CHAPTER 1

INTRODUCTION

1.1 Nanofluidics

Since the invention of carbon nanotubes, confined nanoscale flow of liquid has been the subject of intense research [1, 2, 3, 4]. Interesting physical phenomena have been observed for these very small channels. For example, molecular dynamics (MD) simulation shows that water conducts in short bursts across a very short CNT of diameter 8.1 Å and length 13.4 Å immersed in water, similar to single ion channel activity [1]. Experiments on membranes consisting of CNT's embedded in a film [2] and MD simulation of pressure-driven flow across a single long CNT [3, 4] have also shown flow enhancement (ratio of actual flow rate to the flow rate predicted by continuum theory with no-slip boundary condition at the walls of the CNT's) of the order 10^4 to 10^5 and 10 to 10^3, respectively. Another interesting observation is that the flow transition from continuum to subcontinuum at a CNT diameter between 12.5 Å to 13.6 Å due to slip at the wall and the change from a disorderly structure to orderly structures as the diameter is decreased [3, 4].

In contrast to the flurry of studies on confined nanoscale flow, there have been few studies on the exterior flow past nanoscale objects such as CNT and graphene. Using molecular dynamics simulations, the drag on an array of CNT's in water flow has been calculated and compared to the drag predicted by continuum theory [5, 6]. Deviations are observed [5, 6] and the corrections (the Navier slip boundary condition) introduced in continuum theory have not been satisfactory [6]. The deviations are also explained qualitatively in terms of viscous heating [5, 6]. Similarly, the drag on a single CNT in a uniform liquid argon flow has also been calculated by MD simulations and compared to the drag calculated from finite element simulation and empirical

relation between drag coefficient and Reynolds number[7]. Deviations are again observed but no attempt is made to explain the difference. In the three studies, the change in the structure of the liquid in terms of density layering and viscosity layering in the vicinity of the CNT with flow speed has not been looked into carefully, even though the diameters of the CNT's used (about 10 Å) are small. Because liquid structure has been shown to affect the flow in confined CNT of about the same diameter [3], it is important to look at the fluid structure of exterior flow. As much as we know, there is no study on the flow past a graphene sheet.

1.2 Motivation

The study of exterior flow past nanoscale objects is important not only because the physics can be different from that past macroscopic objects, but also because this flow system is present in a number of promising applications. Arrays of CNT's have been proposed as fins for chip cooling [8] and shape memory alloy cooling [9]. CNT's are said to be a good choice of material for fins because they have very high thermal conductivity and can be made very small[8, 9]. The higher the thermal conductivity, the more gradually the fin efficiency (defined as the ratio of the fin heat transfer rate to the heat transfer rate of the fin if the entire fin were at the base temperature) drops with fin length. For a given volume of material, the smaller the fins, the greater the surface area for convective heat transfer to occur. When cooling of the fins is carried out by forcing a fluid such as air past them, knowledge of flow speed variation with pressure becomes important to properly design such heat sinks [10]. Another promising application is the use of CNT's and graphenes as nanoresonators for mass measurement [11, 12]. This application requires nanoresonators to operate in a fluidic environment [11, 13]. Physical models for the vibration of resonators need the drag coefficient on the resonator to estimate the damping coefficient [14, 15]. Allowing a solution of hydrochloric acid to flow past a piece of graphene to generate electricity [16] is also an example of an exterior flow over a graphene sheet.

The overarching goal of this study is to introduce corrections such that the fluid dynamics in this flow system can be modeled by continuum theory. This is important because MD simulations of this system are computationally ex-

pensive and therefore, are not feasible engineering design tools. On the other hand, continuum simulation tools such as Computational Fluid Dynamics (CFD) and the Finite Element Method (FEM) are very well-established engineering design tools which are much more computationally affordable.

1.3 Overview

This thesis is broken up into chapters that contribute to different aspects of our study. Chapter 2 describes the details and setups of our MD simulations. The background of MD can be found in many good textbooks (see for example [17]). Chapter 3 discusses the liquid argon flow past an array of CNT's. We compare the drag coefficients calculated from MD simulations and that calculated using Stokes equation. Chapter 4 discusses the liquid argon and SPC/E water flow past a graphene sheet. We first describe a modified method to generate uniform flow at a boundary of the MD domain and we discuss some advantages of this method over the original method. We then compare the drag coefficients calculated by MD, CFD and matched asymptotic analysis of the Navier-Stokes equation in an unbounded uniform flow. We also compare the velocity profile calculated by MD and CFD. Chapter 5 summarizes the important results of our study.

CHAPTER 2

MOLECULAR DYNAMICS SIMULATION DETAILS

The Large-scale Atomic/Molecular Massively Parallel Simulator (LAMMPS) is used to simulate the flow past a CNT and a graphene sheet[18].

2.1 Flow past CNT

Figure 2.1 shows the setup to simulate flow past CNT. The size of the domain is $220 \times 220 \times 21.3$ Å^3. In the middle of the domain is a (12,0) CNT of diameter 9.3946 Å and length 21.3 Å. The carbon atoms of the CNT are frozen to their equilibrium position at zero temperature as it is customarily done to facilitate the analysis of slip velocity[19, 5, 6]. The CNT is surrounded with argon atoms whose pairwise interaction between atoms i and j are described by the Lennard Jones potential

$$E_{ij} = 4\epsilon_{Ar}\left[\left(\frac{\sigma_{Ar}}{r_{ij}}\right)^{12} - \left(\frac{\sigma_{Ar}}{r_{ij}}\right)^{6}\right] \tag{2.1}$$

The pairwise interaction between an argon atom and a carbon atom is also specified by the LJ potential with σ_{Ar} and ϵ_{Ar} replaced by σ_{ArC} and ϵ_{ArC}. In this study, we set $\sigma_{ArC} = \sigma_{Ar}$ for all simulations. For liquid argon, $\epsilon_{Ar} = 0.01032$ eV and $\sigma_{Ar} = 3.405$ Å [20].

The time step is set to 1 fs. The system is equilibrated for 1 ns at 96 K by applying the Nosé-Hoover thermostat [21, 22] in all directions. The flow is driven by applying a uniform acceleration (or equivalently force) to all argon atoms. As a result, the flow is equivalent to a gravity or pressure-driven flow. When the acceleration is applied, the Nosé-Hoover thermostat is only applied in the axial or z-direction of the CNT. This ensures that the flow velocity components in the x- and y- directions do not introduce biasness in the temperature control of the system. This is because when there is non-

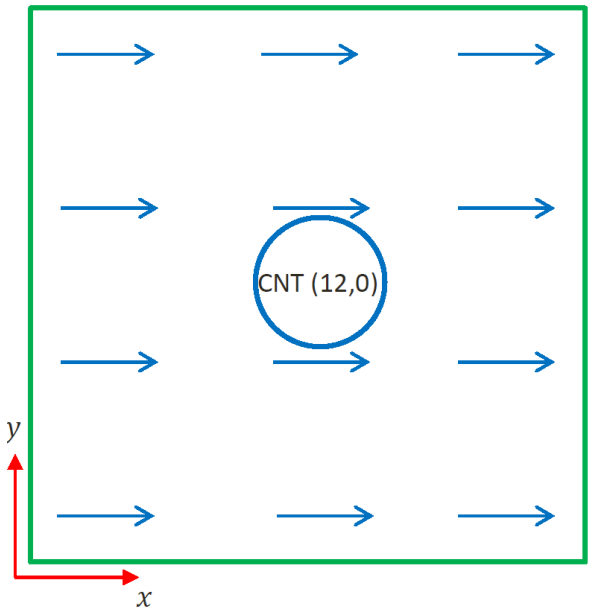

Figure 2.1: Simulation setup of liquid argon-CNT system

zero flow velocity in a particular direction, say x, the x-component of the mean velocity of atoms in a given region is also non-zero. If we calculate the temperature in that region using the velocity components in all directions, we need to subtract the mean velocity from the velocity of each atom in the region. Because this kind of calculation may depend on the size of the region and the sampling duration to obtain good statistics, we avoid this situation by just applying the thermostat in the direction where there is no flow or the z-direction.

The boundary conditions are periodic in all directions. In other words, atoms exiting at one end of the boundary will return at the other end. For computational efficiency, interaction beyond $2.5\sigma_{Ar}$ of an atom is neglected. Due to the periodic boundary conditions, we emphasize that the system is equivalent to a square-periodic array of cylinders, even though only one CNT is simulated at one time.

At steady state, the force acting on the CNT can be calculated by summing up the forces on all the fluid atoms. This is straightforward since the applied acceleration is known. The average velocity is calculated as the average velocity over all fluid atoms in the domain. For a given set of parameters, the simulation is repeated twice as there is little difference in the average velocity between runs. The simulations were run for 30 ns after equilibration. The

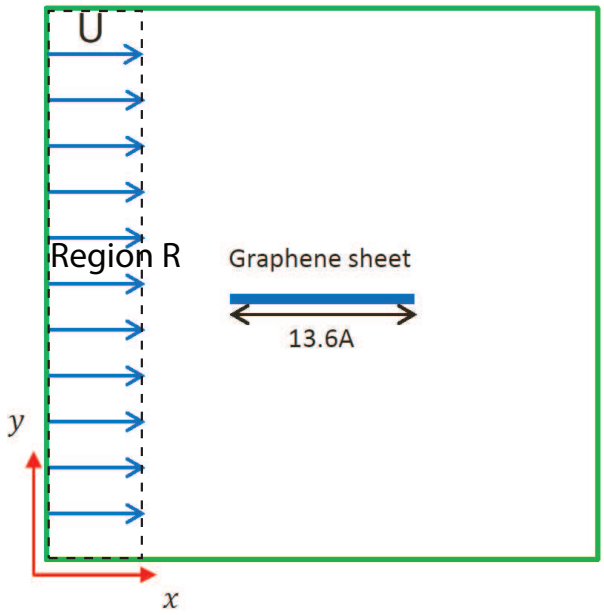

Figure 2.2: Simulation setup of liquid argon-CNT or water-CNT system

production run is the last 20 ns of a simulation.

The dynamic viscosity of liquid argon in the flow past CNT is $\mu = 0.2005$ mPa.s, obtained as the average of two major studies [23, 24] at a reduced temperature of $T^* = \frac{k_B T}{\epsilon_{Ar}} = 0.801$ and reduced density of $\rho^* = \rho\sigma_{Ar}^3 = 0.799$.

2.2 Flow past Graphene Sheet

Fig. 2.2 shows the setup of our simulation of flow past a graphene sheet. In the middle of the domain is a graphene of size 13.528×21.3 Å^2. The graphene atoms are also frozen. We simulate two kinds of liquids - argon and SPC/E water [25]. The length of the domain in the z-direction is always 21.3 Å for all graphene simulations. So only the domain lengths in the x- and y- directions are reported throughout the rest of the paper.

The interaction between liquid argon atoms and between liquid argon atoms and graphene atoms are also specified by LJ potentials. The time step is 1 fs. The system is equilibrated for 1 ns at 96 K by applying the Nos é-Hoover thermostat in all directions.

The dynamic viscosity of liquid argon in the flow past graphene sheet is $\mu = 0.217$ mPa.s, obtained as the average of two major studies [23, 24] at a

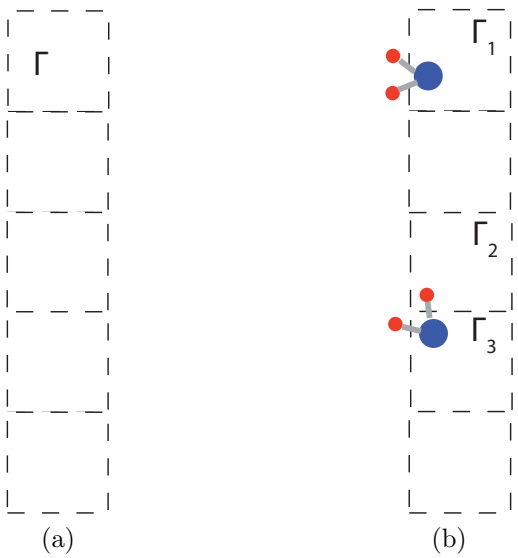

Figure 2.3: (a) Partitioning of region R into subregions. (b) Special cases in SPC/E water simulation.

reduced temperature of $T^* = 0.801$ and reduced density of $\rho^* = 0.807$.

We impose a uniform velocity U in the region R of width 10 Å as indicated in the figure. We modify the method of Walther [5, 26] to achieve uniform velocity in the region. The idea of this method is to partition region R where we want to impose a velocity $\mathbf{V}$ into a smaller number of subregions (such as Γ) as shown in Fig. 2.3a. In each subregion, a uniform body force or acceleration is applied to ensure that the center of mass velocity of the subregion converges to $\mathbf{V}$ eventually. First, the center of mass velocity, v_{cm} of a subregion is sampled over a number of time steps, N_t instead of every time step. Let N_c be the total number of atoms which were in the subregion over a sampling period from time step t_1 to $t_{N_t}$and $\mathbf{v_i}$ be the velocity of each atom. Then $\mathbf{v_{cm}^{(1)}}$, the center of mass velocity over the sampling period is given by

$$\mathbf{v_{cm}^{(1)}} = \frac{1}{N_c} \sum_{i}^{N_c} \mathbf{v_i} \tag{2.2}$$

Sampling over a period of time instead of each time step reduces the error in $\mathbf{v_{cm}}$.

Concurrently, the center of mass acceleration, $\mathbf{a_{cm}^{(1)}}$ just due the LJ interactions is also sampled in the same way, i.e., it is given by

$$\mathbf{a_{cm}^{(1)}} = \frac{1}{N_c}\sum_{i}^{N_c}\mathbf{a_i} \tag{2.3}$$

Let δt be the step size. Over the the next N_t time steps, a uniform acceleration $\mathbf{a_{app}^{(2)}}$ given by

$$\mathbf{a_{app}^{(2)}} = \frac{\mathbf{V} - \mathbf{v_{cm}^{(1)}}}{N_c \delta t} - \mathbf{a_{cm}^{(1)}} \tag{2.4}$$

is applied to all atoms in the subregion.

This process is repeated every N_t time steps and independently in each subregion. The center of mass velocity and acceleration $\mathbf{v_{cm}^{(\alpha)}}$ and $\mathbf{a_{cm}^{(\alpha)}}$ for the time steps $t_{(\alpha-1)N_t}$ to $t_{\alpha N_t}$ are used to calculate the applied acceleration $\mathbf{a_{app}^{(\alpha+1)}}$ over the next block of time steps $t_{\alpha N_t}$ to $t_{(\alpha+1)N_t}$.

We also use SPC/E water in our study. The time step is 1 fs. The system is first equilibrated at T=298K and a pressure of 1 bar as an NPT ensemble[27, 28, 29]. During equilibration, only the box lengths in the x- and y- directions are allowed to change.

The LJ interaction potential is specified only between oxygen atoms of the water molecules and between oxygen atoms of water molecules and the graphene atoms. The parameters for the former are $\sigma_{OO} = 3.1656$ Å and $\epsilon_{OO} = 0.15539$ kcal/mol [25] and parameters for the latter are $\sigma_{OC} = 3.19$ Å and $\epsilon_{OC} = 0.09369$ kcal/mol [30].

The dynamic viscosity of SPC/E water is taken as 0.729 mPa.s from a study by González and Abascal [31].

When applying the velocity control method for liquid argon to SPC/E water molecules, a complication arises in two cases - (i) one part of the water molecule is in one region Γ_1 (see Fig. 2.3b)and another part is outside region R and (ii) the water molecule is simultaneously in two subregions Γ_2 and Γ_3 (see Fig. 2.3b) and part of it may also lie outside region R. To maintain the rigid bonds and angle of a water molecule, the same accelaration must be applied to all the atoms of the molecule. Thus, for case (i), the applied acceleration on Γ_1 is applied to the whole molecule. For case (ii), the average of the applied accelerations on Γ_2 and Γ_3 is applied to the water molecule. The case of the water molecule spanning more than 2 subregions is impossible

in our simulation because the size of the subregion is always larger than that of a water molecule.

The force acting on the graphene sheet is calculated by summing up the forces between the graphene atoms and the fluid atoms. The error in a quantity is given by

$$\epsilon = t_{\alpha,n-1}\frac{S_n}{\sqrt{n}}, \tag{2.5}$$

where S_n is the sample standard deviation. $t_{\alpha,n-1}$ is defined as

$$P(T < t_{\alpha,n-1}) = \alpha\% \tag{2.6}$$

T is the random variable with a t-distribution of degree of freedom $n-1$. Let $< O >$ be the sample mean. Then $< O > \pm\epsilon$ is a $(100-2\alpha)\%$ confidence interval for the true mean. For a given set of parameters, unless specified otherwise, the simulation is repeated 4 times, i.e., $n = 4$ with different initial velocities and the average of the results is presented here. We choose $\alpha = 2.5$.

CHAPTER 3

FLOW PAST AN ARRAY OF CNT'S

The flow past an array of CNT's has been investigated for three cases of the interaction parameter between a liquid argon atom and a carbon atom (A) $\epsilon_{ArC} = 1.5\epsilon_{Ar}$ (B) $\epsilon_{ArC} = \epsilon_{Ar}$ and (C) $\epsilon_{ArC} = 0.5\epsilon_{Ar}$.

We compare the drag coefficients calculated by MD and that calculated by continuum theory. In the continuum theory, the flow is described by the Stokes equation and the objects are square periodic array of cylinders. An expression for the drag has been obtained by Hasimoto [32] in powers of volume fraction of the cylinder, ϕ (defined as the ratio of the volume of the cylinder to the volume of the domain) and subsequently extended by Sangani and Acrivos [33] to higher powers of ϕ. The formula obtained by Sangani and Acrivos is given by

$$\frac{1}{C_d} = \frac{Re}{8\pi}\left(-\frac{1}{2}\ln\phi - 0.738 + \phi - 0.887\phi^2 - 2.039\phi^3\right), \qquad (3.1)$$

where $C_d = 2F/\rho < U >^2$ and $Re = \rho < U > D/\mu$ are the drag coefficient and the Reynolds number respectively. $< U >$ is the average flow velocity across a unit cell.

To obtain agreement between the drag coefficients calculated by MD and that calculated by Eq. 3.1, we need to use the effective radius of the cylinder instead of the nominal radius of the cylinder (the distance from the center of the CNT to the surface of CNT). To get the effective radius, we look at the average density profiles around the CNT obtained by partitioning the region into radial bins as shown in Fig. 3.1. The size of the bins in the radial direction for all density profile calculation is $0.03\sigma_{Ar}$. The number of atoms in each bin is counted every 1000 time steps over the course of the production run of a simulation and averaged over the number of sampling time steps to

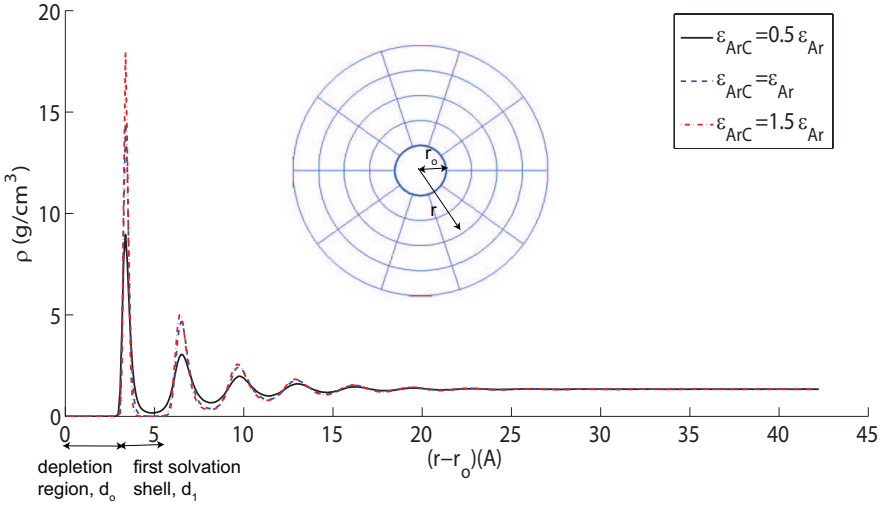

Figure 3.1: The radial density profile around a CNT in a liquid argon-CNT system without any applied acceleration for different interaction parameters.

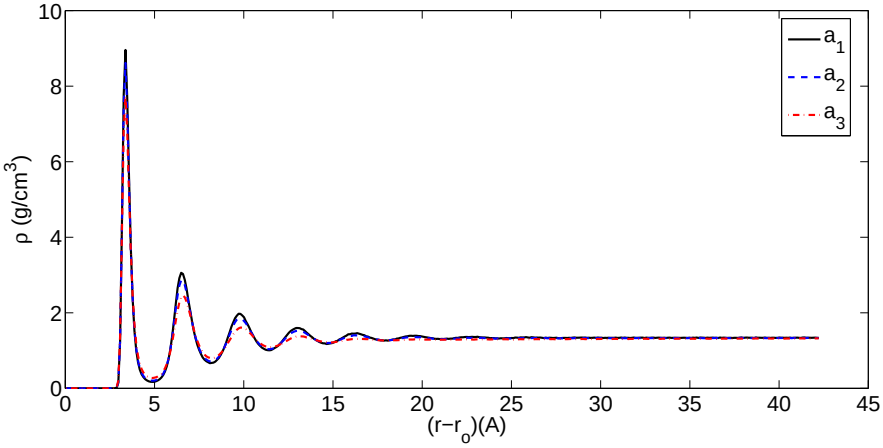

Figure 3.2: The radial density profile around a CNT in a liquid argon-CNT system without applied acceleration and with different applied acceleration. In unit of A/(ps)^2, the applied accelerations are $a_1 = 0$, $a_2 = 1.16 \times 10^{-3}$ and $a_3 = 2.32 \times 10^{-3}$.

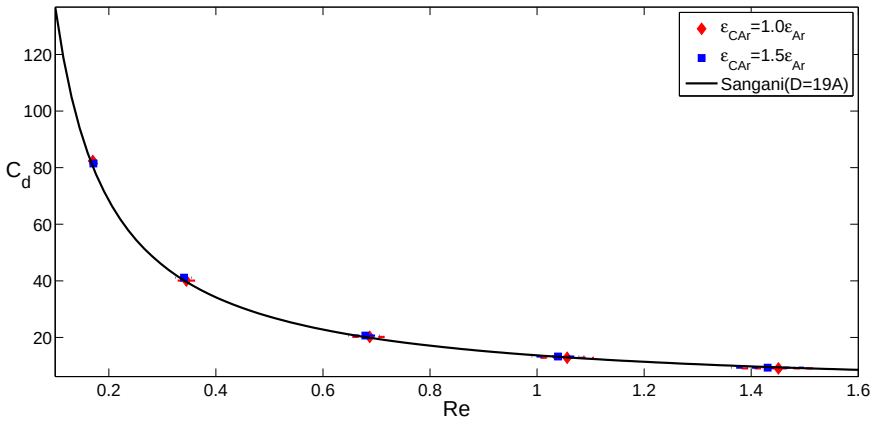

Figure 3.3: The drag coefficients for cases (A) and (B) compared to the Sangani curve calculated by Eq. 3.1 with $D = 2(r_o + d_o + d_1)$.

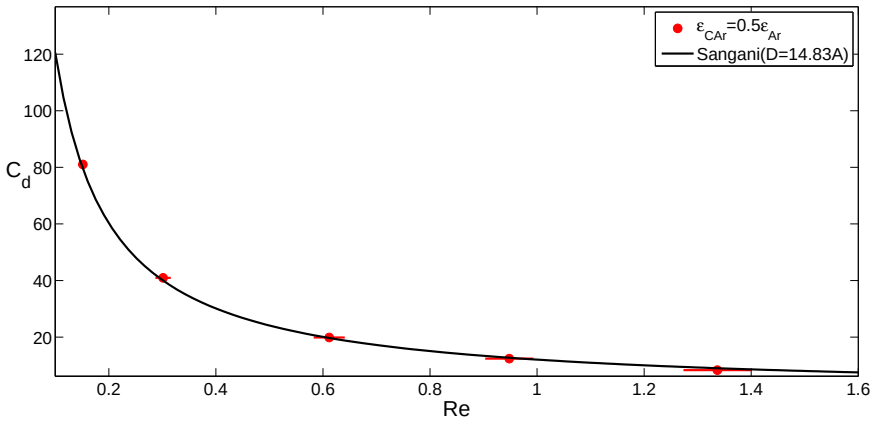

Figure 3.4: The drag coefficients for the case (C) compared to the Sangani curve calculated by Eq. 3.1 with $D = 2(r_o + d_o)$.

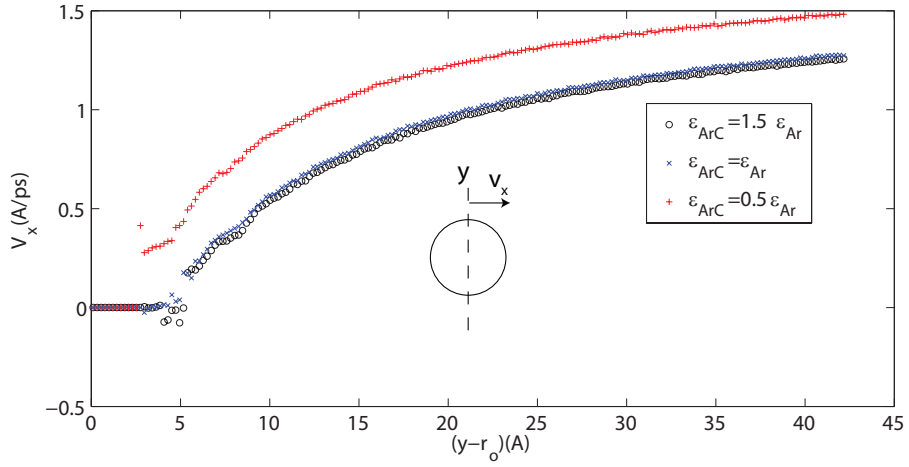

Figure 3.5: The tangential velocity along the y-direction across the center of the CNT for cases (A),(B) and (C)

.

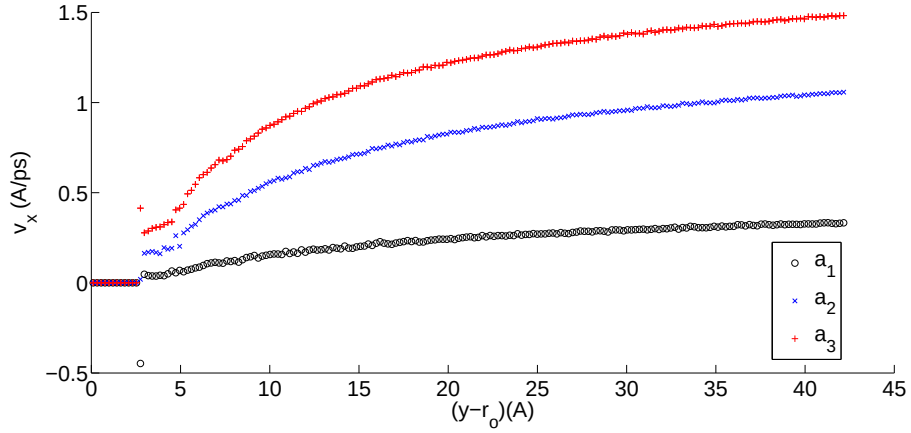

Figure 3.6: The tangential velocity along the y-direction across the center of the CNT for case (C) and different accelerations. In unit of $\mathrm{A}/(\mathrm{ps})^2$, the applied accelerations are $a_1 = 5.793 \times 10^{-4}$, $a_2 = 1.74 \times 10^{-3}$, $a_3 = 2.32 \times 10^{-3}$

obtain the average density profile. As found in our simulations, the density profile is essentially axisymmetric. Hence we only look at the radial density profile. Fig. 3.1 shows the density profiles surrounding a CNT for cases A, B and C with no applied acceleration. There are two regions surrounding the CNT which are important to our discussion (refer to Fig. 3.1). The depletion region is a region where no fluid atom can go due to the repulsive van der Waals interaction at close range. The first coordination shell is the region between the end of the depletion region and the first minimum of the density profile plot. As can be seen, the layering or fluctuation in the density is smeared out as the interaction parameter decreases in strength. When the applied acceleration is increased, Fig. 3.2 shows that the fluctuation in density decreases. However, the positions of the maxima and minima are essentially unchanged. The small change in the liquid structure allows us to define a single effective diameter that works for the range of velocity considered in this work.

Fig. 3.3 shows the comparison between drag coefficients calculated by MD and drag coefficients calculated by Eq. 3.1 using an effective diameter $D = 2(r_o + d_o + d_1)$, where d_1 includes both the depletion region and first coordination shell. The calculated volume fraction is $\phi = \pi D^2/(4L^2) = \pi \times 19^2/(4 \times 220^2) = 0.0069$. Eq. 3.1 has been shown to work very well for $0.001 \leq \phi \leq 0.2$ (see [34]). The agreement between the two results is very good. The reason for including the first solvation shell is that this layer of fluid is at a very high viscosity (due to its higher density) compared to the rest of the fluid and thus behaves more like a solid. This fact can also be inferred from the velocity profile around the CNT. For simplicity, in Fig. 3.5 we look at the tangential velocity along the direction perpendicular to the flow and through the center of the CNT.

Fig. 3.4 shows the comparison between drag coefficients calculated by MD and drag coefficients calculated by Eq. 3.1 using an effective diameter $D = 2(r_o + d_o) = 14.83$, where d_o includes only the depletion region. The volume fraction is 0.0036, well within the range where Eq. 3.1 is shown to work well. There is also good agreement between the two results. At the highest Re, the MD drag coefficient is slightly below the Sangani drag coefficient, even though the effect of inertia is to increase the drag coefficient [35]. This is due to the fluid slipping at the surface of CNT as shown in Fig. 3.6. The velocity profile is calculated using a bin size of $0.065\sigma_{Ar}$ in

the radial direction and $\pi/5$ rad in the angular direction. As expected, the slip increases as the applied acceleration is increased. We do not attempt to provide the slip correction to Eq. 3.1 because the deviation between the MD drag coefficient and Sangani drag coefficient is small even for weak fluid-solid interaction.

CHAPTER 4

FLOW PAST A GRAPHENE SHEET

4.1 Evaluation of the velocity control method

We compare the original velocity control method by Walther et al. [5, 26] (method A) and the modified method we use in this study (method B) in terms of the temperature profiles and the velocity profiles using a domain of size 300×300 Å^2. The velocity control methods are applied to a region R as shown in Fig. 2.2. The region R has thickness of 10 Å in the flow direction and it is partitioned into subregions of 10×10 Å^2 in the y-direction. For method B, we set $N_t = 500$. Setting N_t to be too small will produce the artifacts associated with method A. On the other hand, setting N_t too large will cause the uniform velocity in region R to be significantly less than the desired uniform velocity. Fig. 4.1 shows the temperature profiles of methods A and B. The temperature T_z is calculated by the formula $\frac{1}{k_B}\sum_i m_i v_{z,i}^2$, where k_B, m_i and $v_{z,i}$ are the Boltzmann constant, the mass of atom i and the z-component of atom i velocity, respectively. Method A generates a maximum temperature difference of about 20 K in the domain. The temperature gradient in region R in the flow direction is also large compared to the rest of the domain. In contrast, method B only generates a small temperature difference of less than 6 K and negligible temperature gradient is seen in the region R. Furthermore, method A also shows undesirable artifact in the velocity profile as shown in Fig. 4.2. There appears to be a steep change in the velocity in region R. On the other hand, the velocity profile obtained by method B gently approaches the uniform velocity in region R. One possible reason why method A produces a steep temperature gradient is because it does not allow the atoms in the subregions enough time to come into equilibrium with the surrounding atoms. In fact, it is equivalent to resetting the velocity every time step as was done in another study [7]. However, we note

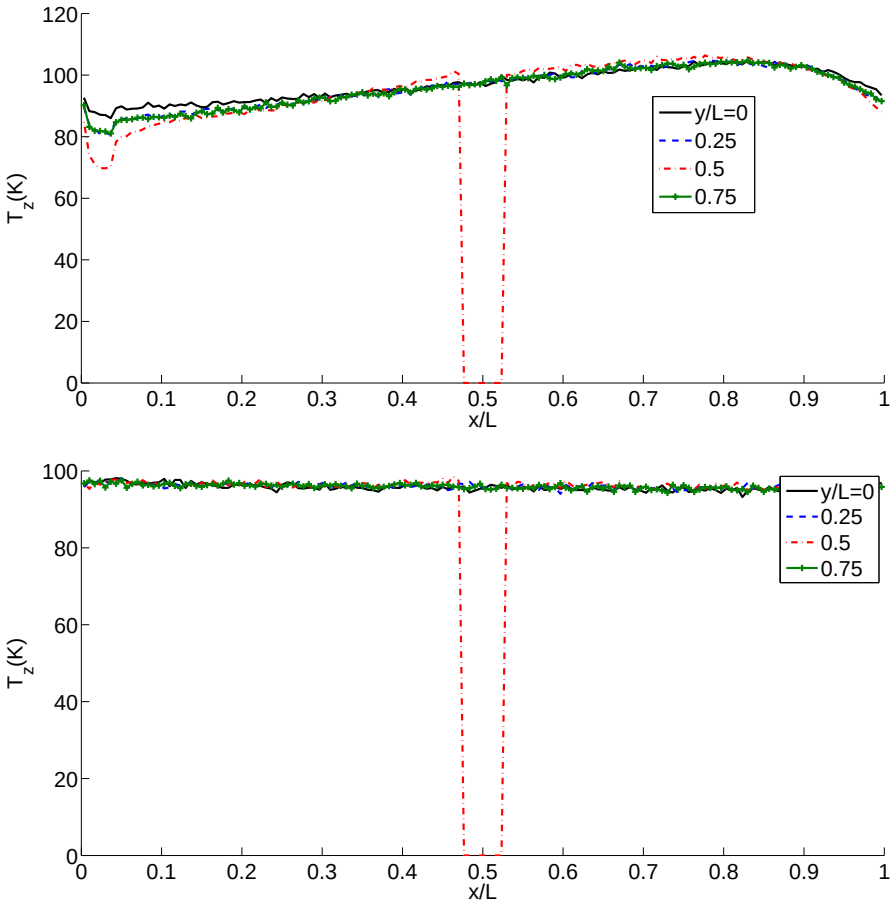

Figure 4.1: Comparison of temperature profiles calculated by method A and method B using bins of size 2×2 Å^2.

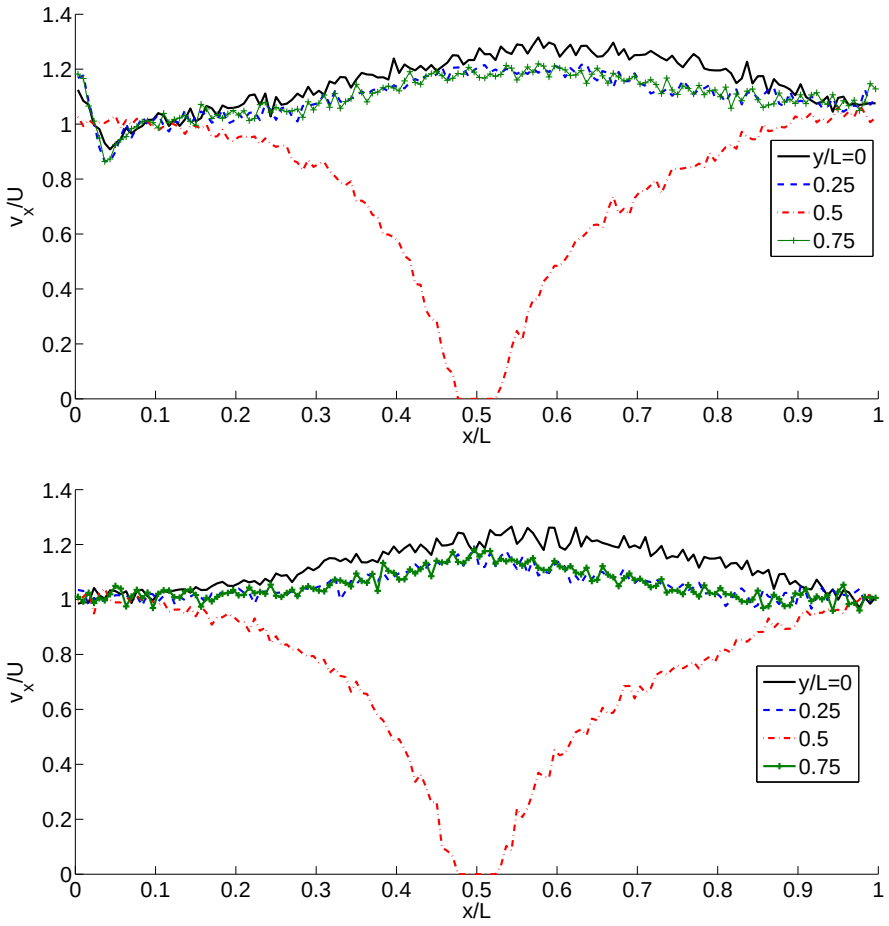

Figure 4.2: Comparison of velocity profiles calculated by method A and method B using bins of size 2×2 Å^2.

that it is possible to reduce the artifacts of method A by using a sufficiently large subregion. We have found that using a subregion of size 20×20 Å^2 is sufficient to reduce the temperature difference to less than 8 K while a subregion of size 40×40 Å^2 is required to remove the artifact in the velocity profile in region R. We also note in passing that it is important to partition region R into sufficiently small subregions so that a uniform velocity is maintained throughout the region R. If only the center of mass velocity of region R as a whole is controlled, then there will be variation in the velocity in the region. For example, the part of the region R directly in front of the object will have a lower velocity compared to the rest of region R.

4.2 Drag coefficient

The uniform flow of liquid argon past a single graphene sheet has been investigated for 2 cases of the liquid-solid interaction parameter (I) $\epsilon_{ArC} = \epsilon_{Ar}$ and (II) $\epsilon_{ArC} = 0.5\epsilon_{Ar}$ each in a domain of size 600×600 Å^2 . The effect of domain size on the drag coefficient will be discussed later.

As discussed before, the first correction we need to provide to continuum theory is the effective shape of the nano-object. To obtain the effective shape, we need to examine the density profile around the graphene sheet. We use a bin size of $0.023\sigma_{Ar} \times 0.023\sigma_{Ar}$. Fig. 4.3 shows the density profile across the center of the graphene in the x- and y- directions for case I. The fluctuation in the x-direction dies down after about 4 peaks compared to 5 peaks in the y-direction. Also, the maximum density in the y-direction is about twice as high as the maximum density in the x-direction. These two observations are due to the weaker interaction between the graphene atoms and the fluid atoms which are located in the x-direction compared to other fluid atoms at the same distance from the graphene in the y-direction. The 2D density profile plot in Fig. 4.5 shows that the depletion region can be approximated by an ellipse of major length $2a$ and minor length $2b$, where $2a$ and $2b$ are as defined in Fig. 4.3. We choose an elliptical shape because the drag coefficient on an ellipse in an unbounded uniform flow is readily available. We use the analytical formula derived by Shintani et al [36] using a matched asymptotic expansion:

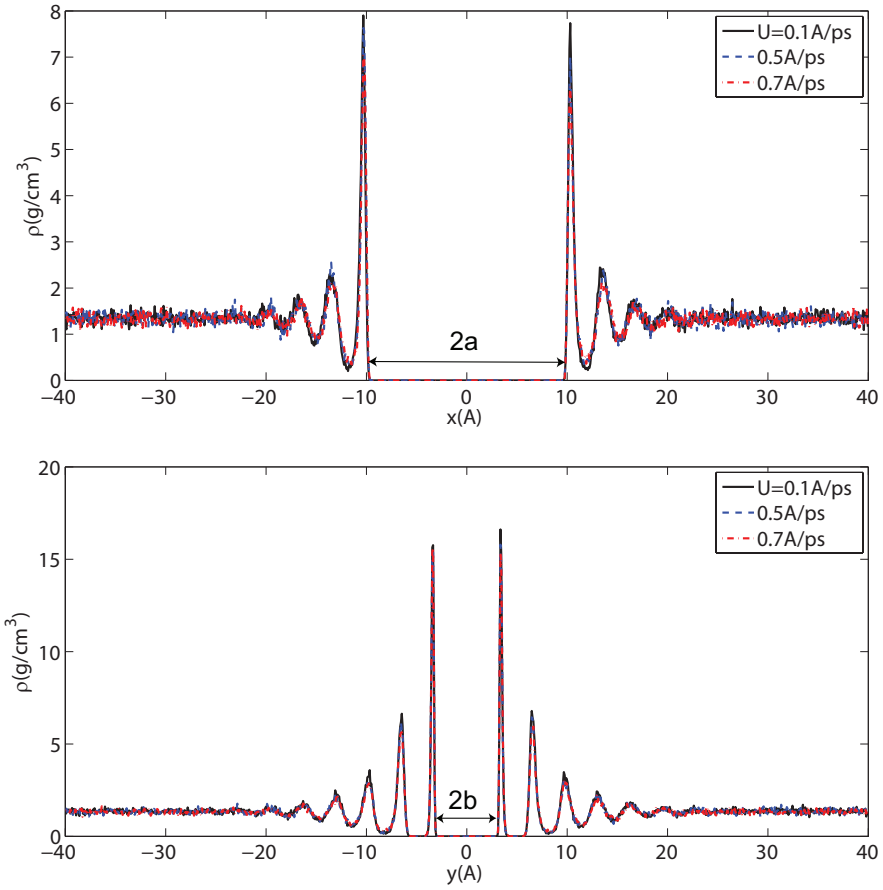

Figure 4.3: The density profile plots along the x- and y-directions through the center of the graphene sheet for case I and different uniform velocities.

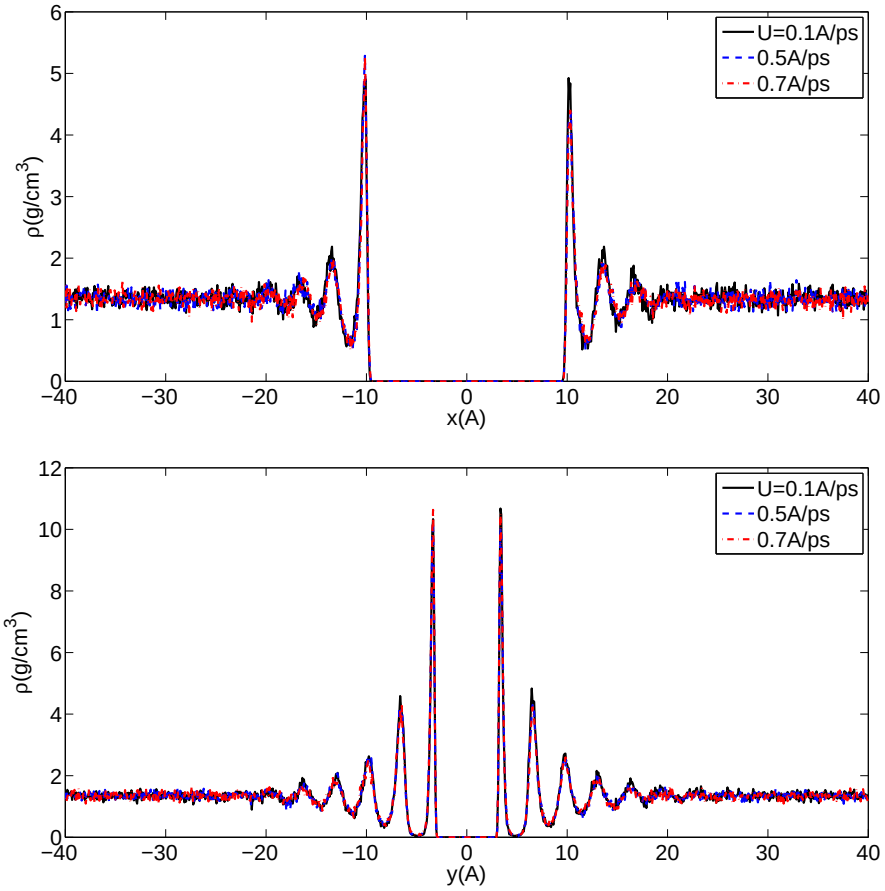

Figure 4.4: The density profile plots along the x- and y-directions through the center of the graphene sheet for case II and different uniform velocities.

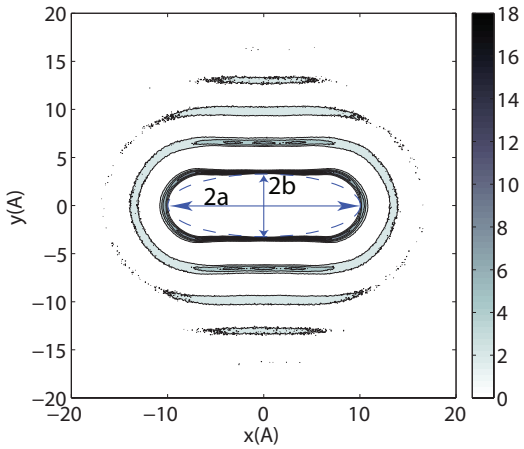

Figure 4.5: The 2D density profile plot for case I and $U = 0.1$A/ps

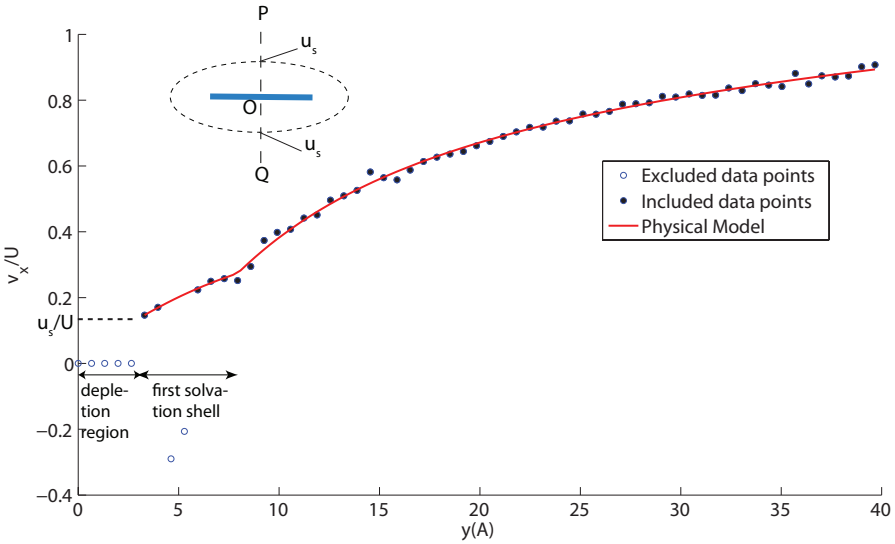

Figure 4.6: The velocity profile v_x through the center of the graphene sheet in the y-direction and the fitted piecewise model of Eq. 4.8.

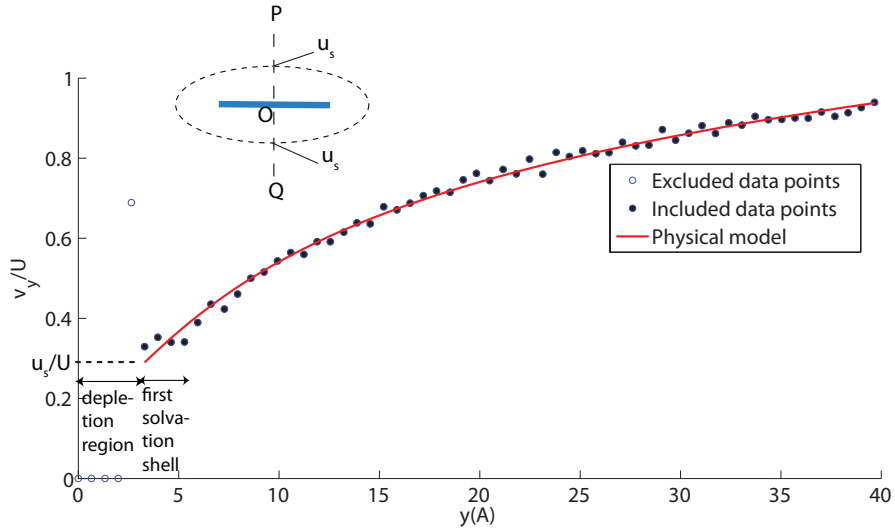

Figure 4.7: The velocity profile v_x through the center of the graphene sheet in the y-direction and the fitted piecewise model of Eq. 4.7.

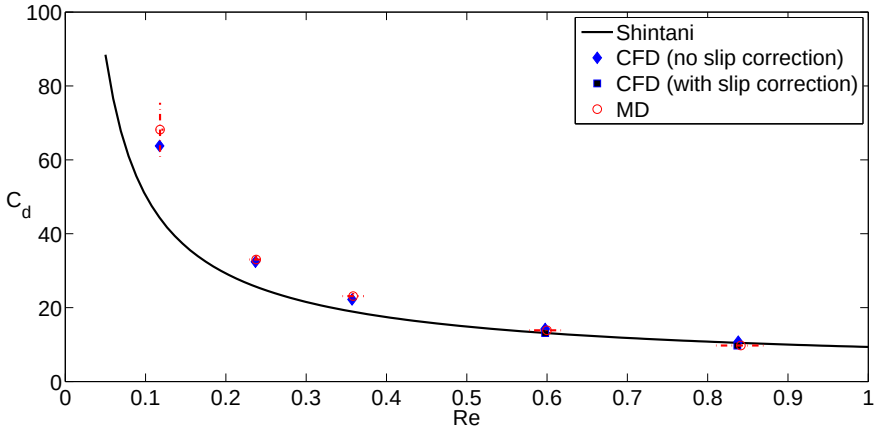

Figure 4.8: The drag coefficients calculated by MD for case I compared to CFD calculation with and without slip correction.

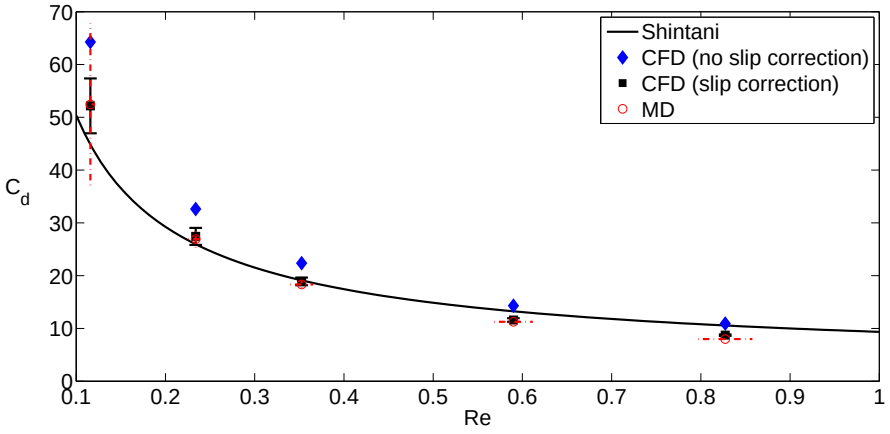

Figure 4.9: The drag coefficients calculated by MD for case II compared to CFD calculation with and without slip correction.

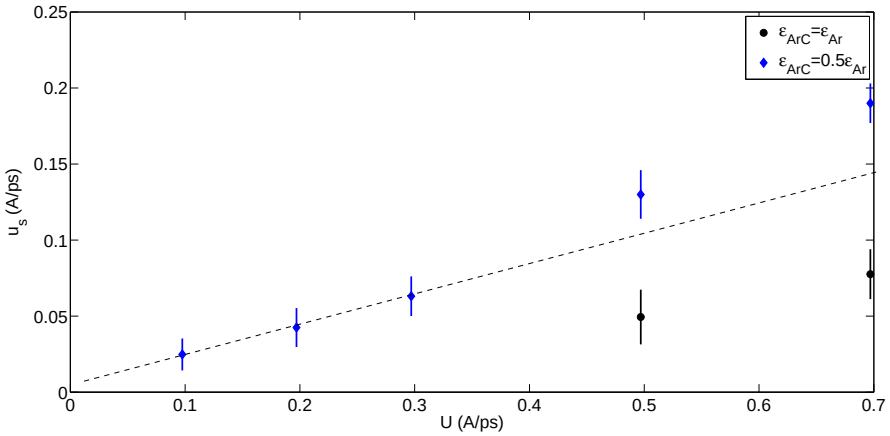

Figure 4.10: The slip velocity versus uniform velocity for cases I and II. The dash line is what the slip velocity would be if there is a linear relationship between slip velocity and uniform velocity.

$$C_D = -\frac{4\pi}{Re}\frac{2\ln Re + 1 + 2\gamma - 8\ln 2 + 2\ln\beta + \left(\frac{\epsilon}{\beta}\right)^2}{(\ln Re - t_+)(\ln Re - t_-)} \tag{4.1}$$

$\epsilon = \frac{\sqrt{a^2-b^2}}{a}$, $\beta = 1+\sqrt{1-\epsilon^2}$ and $t_\pm = -\gamma+4\log 2-\log\beta\pm\frac{1}{2}\left[1+2(\epsilon/\beta)^2+(\epsilon/\beta)^4\right]^{1/2}$.

The second correction which is needed for high Re number or weak interaction parameter is the correction that takes into account slip velocity at the boundary of the effective shape or depletion region. Here we propose a simple correction that could be implemented easily in Computational Fluid Mechanics (CFD). For simplicity, we only look at the slip velocities at the two points of intersection (P and Q) of a line passing through the center O of the graphene sheet parallel to the y-axis as shown by the dashed line labeled PQ in Fig. 4.6. By symmetry, the slip velocities at P and Q are equal. To obtain the slip velocity u_s at any of these points, we take the average of the MD velocity profile along OP and OQ and fit a physical model to the velocity profile. The model is then extrapolated to point P or Q to obtain an estimate of u_s. The physical model we use is derived from a separable solution of the elliptical cylindrical Stokes equation [36]. The elliptical cylindrical Stokes equation is

$$\Delta\frac{1}{h(\xi,\eta)^2}\Delta\psi(\xi,\eta) = 0, \tag{4.2}$$

where $h(\xi,\eta) = \sqrt{\cosh^2\xi - \cos^2\eta}$ and $\Delta = \frac{\partial^2}{\partial\xi^2} + \frac{\partial^2}{\partial\eta^2}$.

A separable solution is

$$\psi = f(\xi)\cos\eta + g(\xi)\sin\eta, \tag{4.3}$$

where $f(\xi) = A_1\xi\cosh\xi + A_2\cosh\xi + A_3\sinh\xi$ and $g(\xi) = B_1\xi\sinh\xi + B_2\cosh\xi + B_3\sinh\xi$.

The relationship between the Cartesian coordinates (x, y) and elliptical cylindrical coordinates (ξ, η) is

$$x = c\cosh\xi\cos\eta \tag{4.4}$$

$$y = c\sinh\xi\sin\eta, \tag{4.5}$$

where $c = \sqrt{a^2 - b^2}$.

The η-component of the velocity is

$$v_\eta = -\frac{1}{h(\xi,\eta)}\frac{\partial\psi}{\partial\xi} \tag{4.6}$$

Since we are only interested in the solution along line PQ, we substitute $\eta = \pi/2$ and replace v_η by v_x in Eq. 4.6 and use Eq. 4.3 to obtain

$$\begin{aligned} v_x &= -\frac{1}{h(\xi,\pi/2)}g'(\xi) \\ &= C_1\xi + C_2 + C_3\tanh\xi \end{aligned} \tag{4.7}$$

Here, C_1, C_2 and C_3 are parameters of the fit. For the strong interaction case I, due to the large first solvation shell (compare Fig. 4.6 and Fig. 4.7), we use a piecewise continuous physical model given by

$$v_x = \begin{cases} C_1\xi + C_2 + C_3\tanh\xi & \xi < \xi_1 \\ C_4\xi + C_5 + C_6\tanh\xi & \xi \geq \xi_1 \end{cases} \tag{4.8}$$

Other than C_i, the location of the discontinuity, ξ_1 is a parameter of the fit. We use the nonlinear-fitting tool available in MATLAB to perform the fitting.

Fig. 4.6 shows the nonlinear-fitting using the model given by Eq. 4.8. The discontinuity in the fit is approximately at the end of the first solvation shell. The gradient of the velocity profile increases with y across the discontinuity,

consistent with the fact that the viscosity of the first solvation shell is higher than the rest of the fluid. This can be deduced from the stress continuity, i.e., $\mu_1 \frac{\partial v_x}{\partial y}|_{y_o^-} = \mu_2 \frac{\partial v_x}{\partial y}|_{y_o^+}$ at $y = y_o$, the position of discontinuity in the velocity gradient.

The slip velocity calculated by extrapolation of the physical model to the boundary of the ellipse is shown in Fig. 4.10. The slip velocity increases linearly with the imposed uniform velocity, U for small U and increases more rapidly for greater U. The slip length is of the order of 1-10 Å and does not remain constant as the imposed velocity is increased. Hence it is inappropriate to use a Navier boundary condition when performing a continuum calculation in this range of imposed velocity. We note that the proper way to determine the slip length is to perform an equilibrium MD simulation and allow the graphene sheet to be flexible [37, 38, 39].

We compare the drag coefficients calculated by MD, Eq. 4.1 and CFD using the same domain size and boundary conditions at the outer boundaries of the domain as in MD. We use the commercially available software FLUENT to do the calculation. A 2D steady-state calculation is performed using a pressure-based solver [40] with second-order momentum upwind scheme. The mesh consists of more than 100000 triangular elements and the convergence of the drag coefficient has been checked by using mesh refinement and meshes of different number of elements. Fig. 4.8 shows the comparison for the strong interaction case I. The drag coefficients calculated by MD agrees very well with that of CFD without any slip correction up Re=0.36. For higher Re, slip correction improves the accuracy of drag coefficients calculated by CFD. However, both CFD and MD appear to overestimate the drag coefficients of an unbounded uniform flow. We later show that the same correction can be applied to Eq, 4.1 to obtain agreement between MD and continuum theory provided that the domain size used for MD simulation is sufficiently large. The drag coefficients for case II also (Fig. 4.9) show very good agreement between MD and CFD with slip correction. The drag coefficient is significantly lower than that without slip for the range of Re considered here.

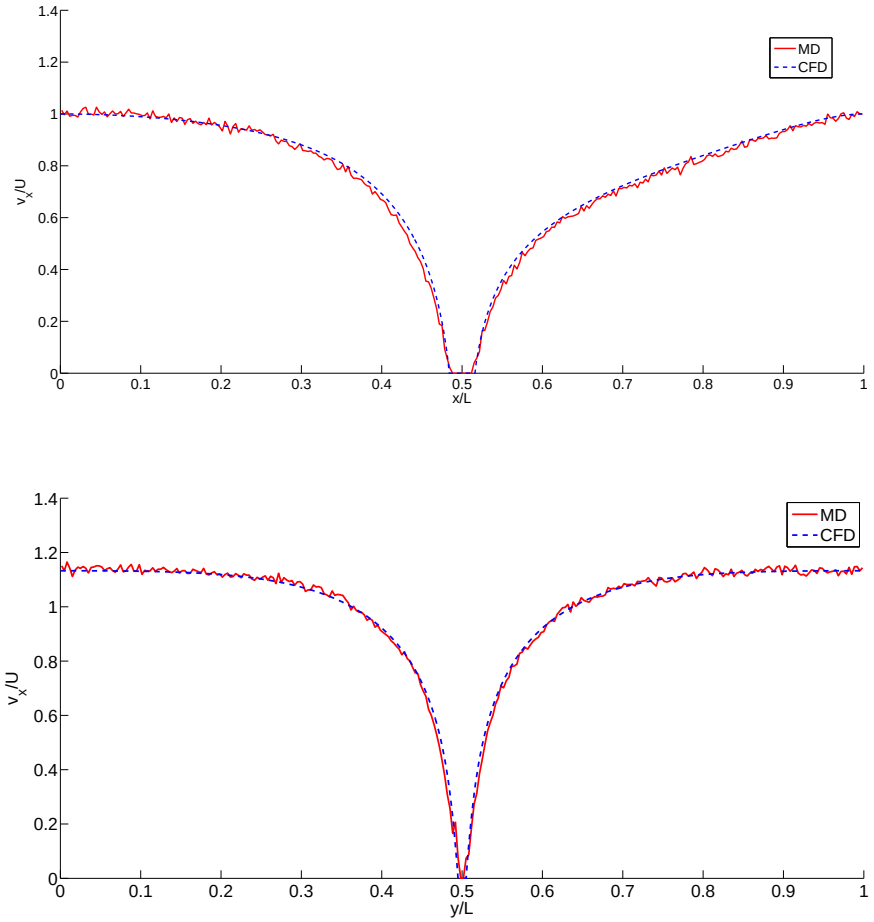

Figure 4.11: Comparison of velocity profiles in the x- and y- directions calculated from MD and CFD for case I. The velocity profile from MD has been calculated with a bin size of 2×2Å. The coordinate has been normalized by the domain size L.

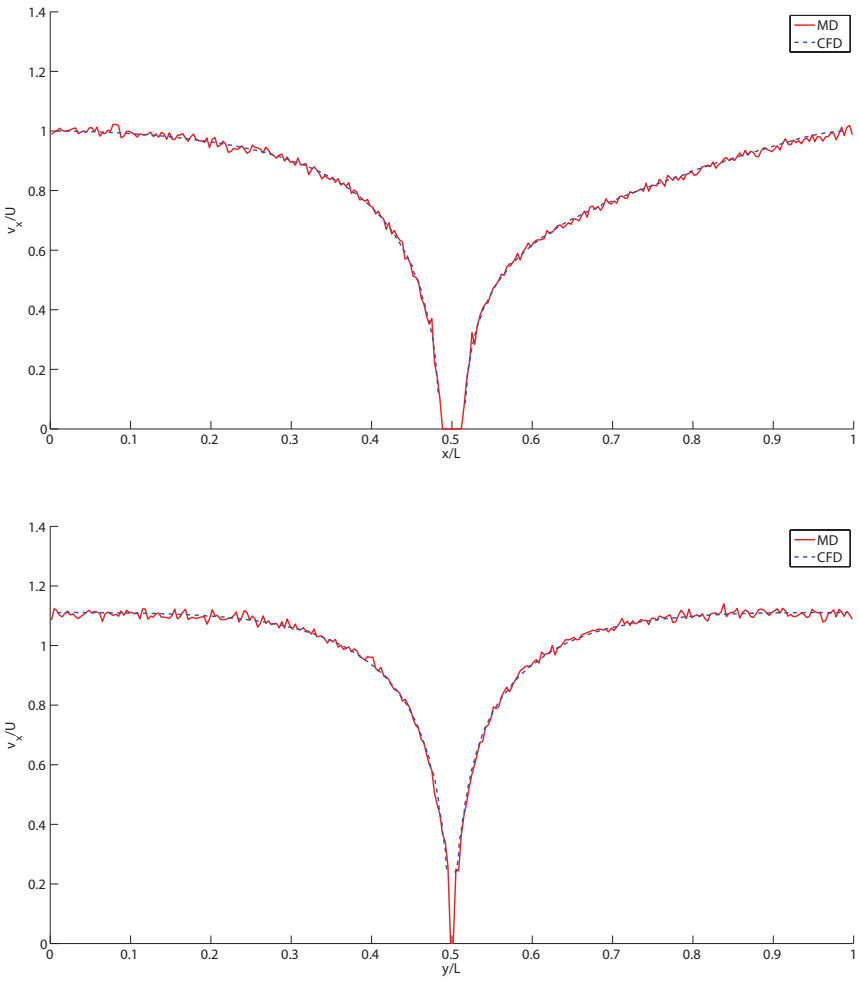

Figure 4.12: Comparison of velocity profiles in the x- and y- directions calculated from MD and CFD for case II.

4.3 Velocity profiles

The drag coefficient is a global quantity of a fluid-solid system. It is instructive to also look at local quantities of the system. Here, we compare the velocity component v_x across the center of the graphene sheet calculated by MD and CFD. For case I, Fig. 4.11 shows that the MD results agree quite well with those of CFD, especially at locations further away from the graphene sheet. However, near the graphene sheet, the prediction of CFD deviates from that of MD. We show in the next section that this deviation could be reduced if we implement the density and viscosity layering surrounding the graphene sheet in CFD. For case II, there appears to be good agreement between MD and CFD throughout the domain, even at locations close to the graphene sheet (see Fig. 4.12). We attribute this to the weaker fluid structure around the graphene sheet, which makes the behavior of the fluid in the vicinity more homogeneous-like.

4.4 Effect of density and viscosity layering

According to Fig. 4.3 and 4.4, the maximum densities are about ρ^* =8.9 and 5.9 respectively in terms of LJ reduced unit. At a reduced temperature $T^* = 0.8$, phase diagram of a LJ system clearly shows that the system exists in a solid phase for $\rho^* \gtrsim 1$ (see [41]). The extremely high density of the first few peaks of Fig. 4.3 and 4.4 does not make physical sense because other than perhaps the first solvation shell, the liquid atoms surrounding the graphene are observed to move freely. Recognizing that this issue arises from our assumption that the atoms are point particles, some authors (see for example, Bitsanis et al. [42]) introduce the concept of local average density (LAD)to describe the behavior of inhomogeneous fluid in terms of a homogeneous fluid. A reasonable choice of a local average density is given by [42]

$$\bar{\rho}(\mathbf{r}) = \frac{6}{\pi\sigma_{Ar}^3} \int_{s<\sigma_{Ar}/2} \rho(\mathbf{r}+\mathbf{s}) \mathrm{d}^3 s \tag{4.9}$$

As shown in Fig. 4.13, the LAD produces a density that has a much weaker fluctuation compared to the original average density. The maximum LAD is slightly greater than 1. Another observation is that the depletion region

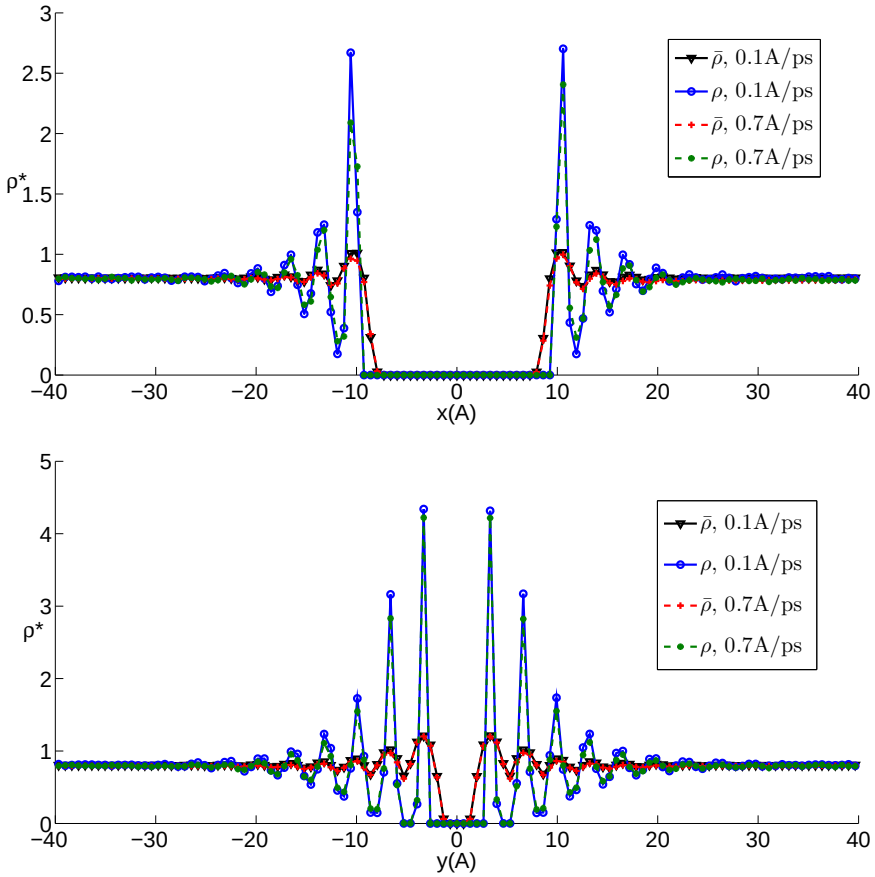

Figure 4.13: Comparison of density profiles and local average density profiles for case I and different velocities.

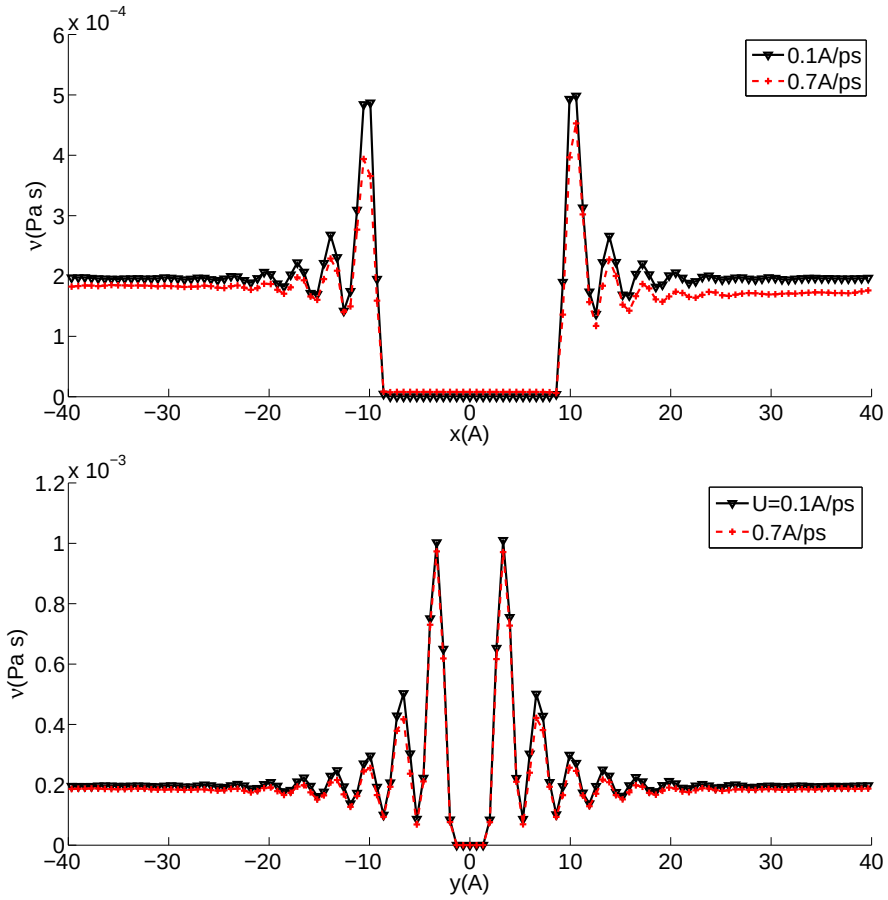

Figure 4.14: Comparison of viscosity profiles for case I and different velocities.

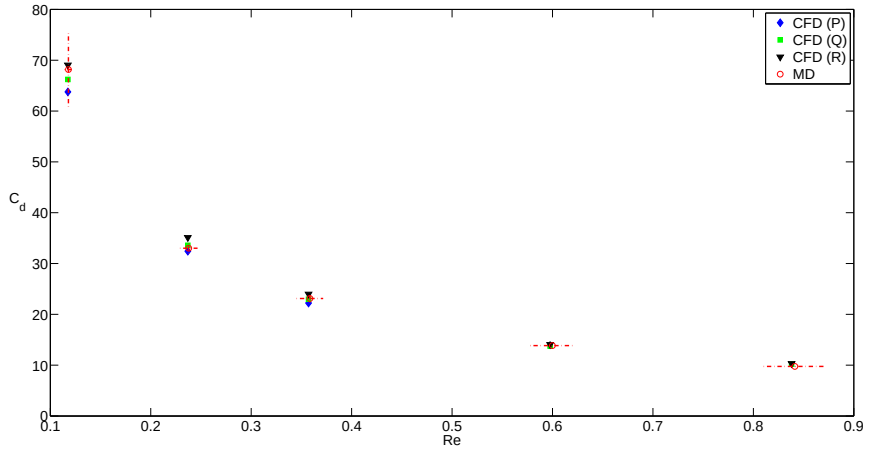

Figure 4.15: Comparison of MD drag coefficients for case I and drag coefficients calculated by CFD for (P) an ellipse (Q) a body with the shape of the depletion region and (R) a body with the shape of the depletion region and density and viscosity layering.

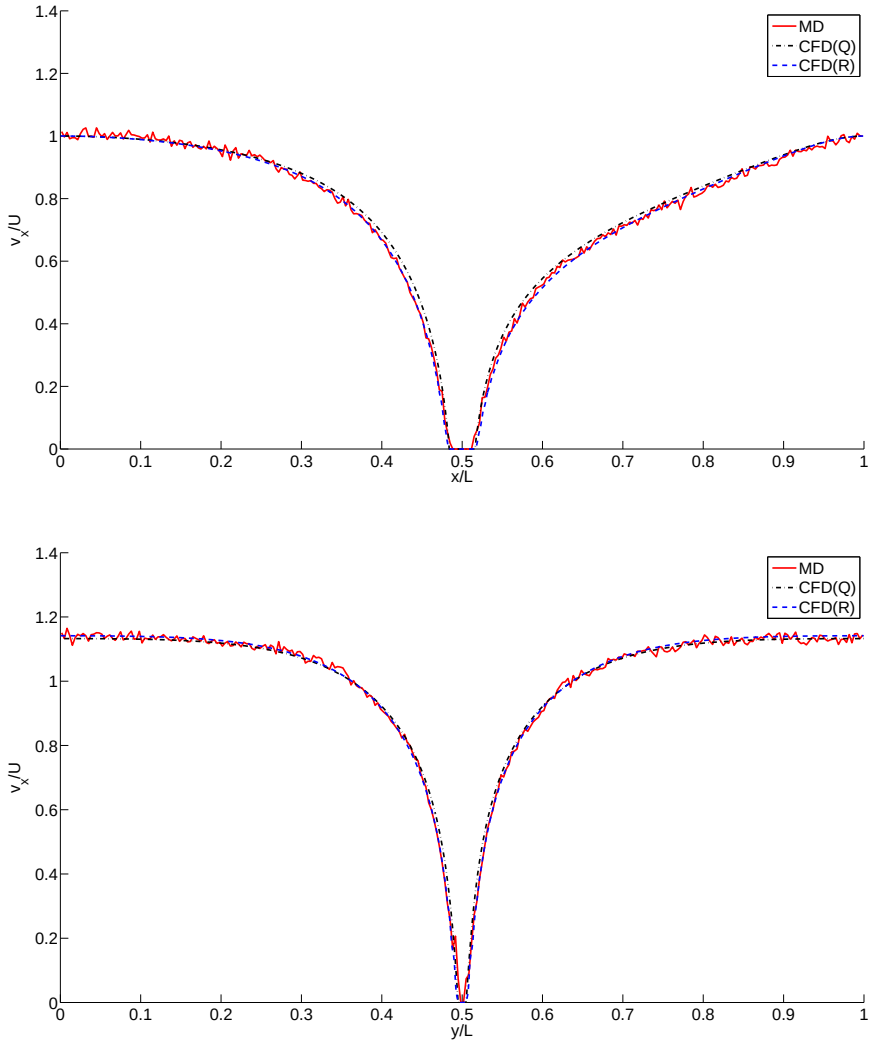

Figure 4.16: Comparison of velocity profiles v_x in the x- and y- directions calculated by MD and CFD (Q) a body with the shape of the depletion region and (R) a body with the shape of the depletion region and density and viscosity layering.

becomes smaller if we look at the LAD.

Once we have the LAD, we can use the viscosity equation of state (viscosity as a function of density and temperature) to calculate the viscosity profile [42]. Our goal is to input the LAD profile and the viscosity profile in FLUENT and examine how the drag coefficients and the velocity profile compare to the case when there are both density and viscosity layering. The viscosity equation of state we choose is the Woodcock viscosity equation of state given by [43]

$$\eta^* = \eta_o^* + \sqrt{2}\eta_o^*(1 - (T^*)^{-4} - T^*/8)\rho^* + C_{AH}(\rho^*)^4/(T^*)^{1/3}, \tag{4.10}$$

where $C_{AH} = 4.8$. The calculation of the zero density viscosity, η_o^* can be found elsewhere [43, 44].

To implement the density and viscosity layering in FLUENT, we have used the actual shape of the depletion region, which can be obtained from the 2D density profile plots such as Fig. 4.5. Fig. 4.15 shows the comparison between the drag coefficients calculated by MD for the strong interaction case and those calculated by CFD with and without layering. Layering appears to increase the drag coefficient slightly. Moreover, we note that approximating the depletion region by an ellipse provides a good estimate for the drag coefficient. By introducing density and viscosity layering into CFD, we note that the agreement of the velocity profile with MD near the graphene sheet improves (see Fig. 4.16).

4.5 Unbounded uniform flow past a graphene sheet

As mentioned previously, the drag coefficients in Fig. 4.8 and Fig. 4.9 suffer from some domain size effect. The lower the Reynolds number, the greater the domain size effect. This could be explained by a simple argument based on the balance of inertia and viscous forces. The viscous force decays away from the object and eventually inertia forces will be dominant. The boundary of the domain should be placed at a minimum distance away from the object where inertial and viscous forces are equal so that at the boundary the velocity of the fluid is close to the upstream velocity. To make this argument

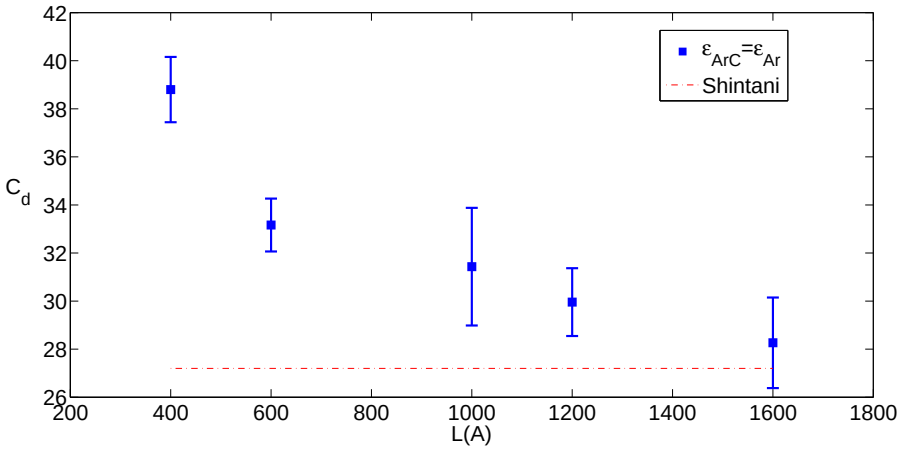

Figure 4.17: Drag coefficient versus domain size for $\epsilon_{ArC} = \epsilon_{Ar}$ and Re=0.24.

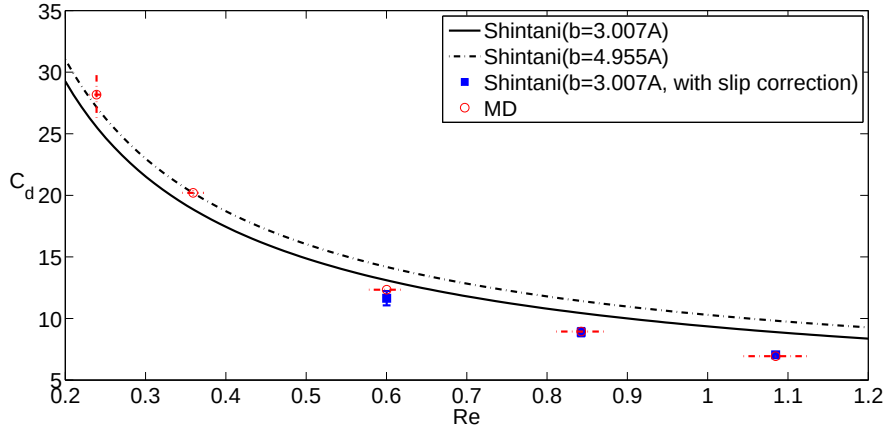

Figure 4.18: Drag coefficient versus Reynolds number for case III compared to that calculated by Eq. 4.1 with and without correction.

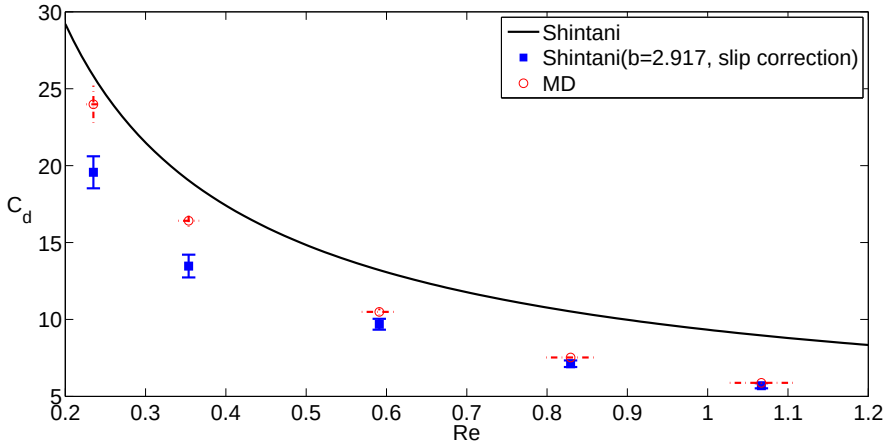

Figure 4.19: Drag coefficient versus Reynolds number for case IV compared to that calculated by Eq. 4.1 with and without correction.

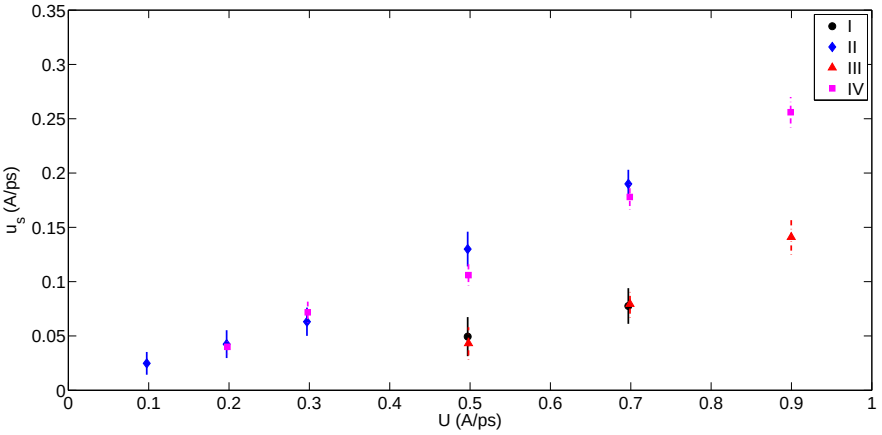

Figure 4.20: Slip velocity versus uniform velocity for cases I, II, III and IV.

more quantitative and to show that this minimum distance depends inversely on Reynolds number, we use the example of an unbounded uniform flow of velocity U over a cylinder of radius r_o. At a radial distance r away from the center of cylinder, the two inertia terms in the incompressible Navier-Stokes equation are $\rho|\frac{\partial \mathbf{u}}{\partial r}| = \frac{\rho U^2 C}{r}$ and $\rho|\mathbf{u}\cdot\nabla\mathbf{u}| = \frac{\rho U^2 C^2}{r}\ln\frac{r}{r_o}$, where C is an arbitrary constant [45]. The viscous term has magnitude $\rho|\nabla^2\mathbf{u}| = \frac{\mu U C}{r^2}$ (see [45]). The first inertia term becomes comparable to the viscous term when $\frac{r}{r_o} = O(\mathrm{Re}^{-1})$ and the second inertia term becomes comparable when $C\frac{r}{r_o}\ln(\frac{r}{r_o}) = O(\mathrm{Re}^{-1})$. Hence, the minimum domain size to approximate an unbounded uniform flow should also be of order Re^{-1}. Moreover, as we have shown previously, the smaller Re, the greater the effect of density and viscosity layering in increasing the drag coefficient (see Fig. 4.15). To examine the issue of domain size effect, we perform the simulations at Re=0.24 with increasing domain size $L \times L$ Å^{2}as shown in Fig. 4.17. The largest domain size 1600×1600 Å^2 is chosen based on the resources available at our disposal. For the rest of this section, the simulation is performed with the largest domain size and two cases (III) $\epsilon_{ArC} = \epsilon_{Ar}$ and (IV) $\epsilon_{ArC} = 0.5\epsilon_{Ar}$. The drag coefficient agrees with the Shintani drag coefficient using a minor axis length which includes both the depletion region and first solvation shell ($b = 4.955$ Å). We also recalculated the drag coefficients and compare them with the Shintani drag coefficient with a simple slip correction. The slip correction is implemented in this manner. Suppose we know from continuum theory with no slip boundary condition that C_d is related to Re by

$$C_d = f(Re) \tag{4.11}$$

where $Re = \frac{UL_c}{\nu}$ and $C_d = \frac{2F_d}{\rho U^2}$. Now consider a system in which there is slip at the boundary. Let u_s be a representative slip velocity. Then the 'true' Reynolds number is

$$Re' = \frac{(U - u_s)L_c}{\nu} \tag{4.12}$$

From Eq. 4.11, the 'true' drag coefficient $C'_D = \frac{2F_d}{\rho(U-u_s)^2}$ is given by

$$C'_D = f(Re') \tag{4.13}$$

The 'nominal' drag coefficient is

$$C_d = \left(1 - \frac{u_s}{U}\right)^2 C'_d = \left(1 - \frac{u_s}{U}\right)^2 f\left(\left(1 - \frac{u_s}{U}\right) Re\right) \tag{4.14}$$

As shown in Fig. 4.18, there is a good agreement between the Shintani results with slip correction and the MD drag coefficients. However, for lower Reynolds number, the MD drag coefficients are closer to the Shintani curve generated with $b = 4.955$ Å. This could be due to both the effects of domain size and the fluid structure close to the graphene.

For the weak interaction case, the simple slip correction also results in agreement between the Shintani results and MD drag coefficients for high Reynolds number. However, it does not work well at low Reynolds number and this may also be due to the domain size effect and the importance of density and viscosity layering at low Reynolds number.

It is also instructive to investigate whether the slip velocities depend on the domain size. Fig. 4.20 shows that the domain size weakly affects the slip velocities for both the strong interaction cases (I and III) and weak interaction cases (II and IV). We also remark that the fluid structure is essentially unchanged for the two domain sizes (600×600 Å^2 and 1600×1600 Å^2) we used in this study. Hence, even without models to predict the fluid structure and the slip velocity, the effective size and the slip velocity corrections can be determined with a moderately large domain size.

4.6 Flow of water past a graphene sheet

To check the robustness of our proposed corrections, the flow of water past a graphene sheet is also simulated with a domain of size 600×600 Å^2 . The corrections, when applied to CFD, result in good agreement with MD (see Fig. 4.21). We also show the predictions of Eq. 4.1 with corrections applied. Assuming that the slip velocity varies slightly with domain size just as the liquid argon case, the predicted drag coefficients would be that of unbounded uniform flow of water past a graphene sheet.

The slip length calculated in this study is of the order of 1-10 Å which is at the low end of the slip lengths reported in the literature [39]. This discrepancy is not surprising because in our study the graphene is frozen

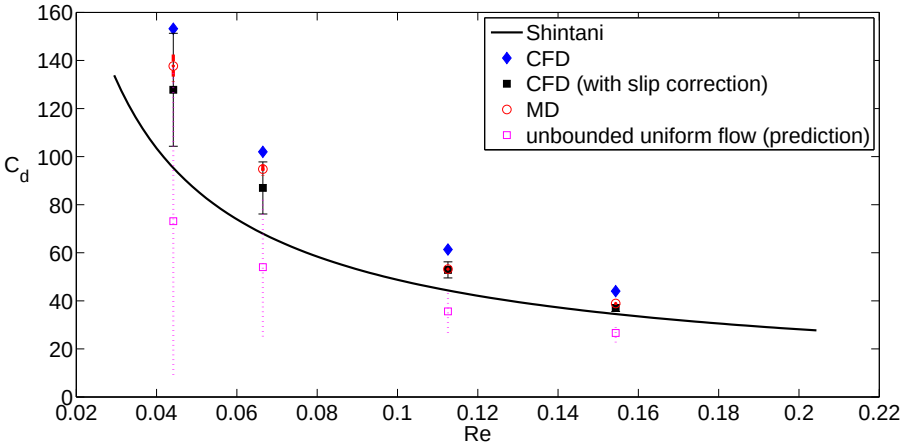

Figure 4.21: Drag coefficients for SPC/E water-graphene system compared to that calculated by CFD with and without correction. Also shown is the prediction for an unbounded uniform flow past a graphene sheet obtained by applying the corrections to Eq. 4.1.

and the fluid is thermostated. We again note that the slip length is not constant and a continuum calculation cannot simply be performed with a Navier boundary condition.

CHAPTER 5

CONCLUSIONS

In this study, we have investigated the exterior flow past an array of CNT and a single graphene sheet. For the flow of liquid argon past an array of CNT, we have found that very good agreement can be obtained between the Sangani analytical expression and MD simulation when an effective diameter is used. In the case of strong interaction $\epsilon_{ArC} = \epsilon_{Ar}$ and $\epsilon_{ArC} = 1.5\epsilon_{Ar}$, the effective diameter includes both the depletion region and the first solvation shell. On the other hand, the effective diameter only includes the depletion region for the weak interaction case $\epsilon_{ArC} = 0.5\epsilon_{Ar}$. For both liquid argon and SPC/E water flow past a graphene sheet, we have also found that good agreement between MD and CFD can be achieved by using an appropriate shape (an ellipse that approximate the depletion region or the exact shape of the depletion region itself) and slip correction. The agreement in the velocity profile near the graphene sheet improves when density and viscosity layering are implemented in CFD. For high Reynolds number, the drag coefficient on a graphene sheet in a very large domain calculated by MD also shows agreement with Shintani analytical result when an ellipse with major and minor lengths equal to the size of the depletion region in the flow direction and normal to the flow direction is used and a simple slip correction is applied to the analytical result.

5.1 Recommended future studies

The next step after this study is to perform the simulation with water and a much larger domain to obtain a drag coefficient which is closer to that of unbounded uniform flow. In the future, such massive amount of resources would be more readily available and allow us to perform the simulations. Another possibility for future study is to check whether the corrections proposed

here will still hold for a flexible graphene. As the graphene size increases, an ellipse will not be a good approximation of the depletion region around the graphene. A rectangular shape would be a more accurate approximation. Unfortunately, as far as we know, there is no known analytical result of the drag coefficient on a rectangular cylinder in the literature. Therefore investigation of the scaling of the drag coefficient with graphene size is also required.

REFERENCES

[1] G. Hummer, J. C. Rasaiah, and J. P. Noworyta, "Water conduction through the hydrophobic channel of a carbon nanotube," *Nature*, vol. 414, pp. 188–190, 2001.

[2] M. Majumder, N. Chopra, R. Andrews, and B. J. Hinds, "Enhanced flow in carbon nanotubes," *Nature Brief Communications*, vol. 438, p. 44, 2005.

[3] J. A. Thomas and A. J. H. McGaughey, "Reaccessing fast water transport through carbon nanotubes," *Nanoletters*, vol. 8, pp. 2788–2793, 2008.

[4] J. A. Thomas and A. J. H. McGaughey, "Water flow in carbon nanotubes: transition to subcontinuum transport," *Physical Review Letters*, vol. 102, p. 184502, 2009.

[5] J. H. Walther, T. Werder, R. L. Jaffe, and P. Koumoutsakos, "Hydrodynamics properties of carbon nanotubes," *Physical Review E*, vol. 69, p. 062201, 2004.

[6] C. Chen, M. Ma, K. Jin, J. Z. Liu, L. Shen, Q. Zheng, and Z. Xu, "Nanoscale fluid-structure interaction: flow resistance and energy transfer between water and carbon nanotubes," *Physical Review E*, vol. 84, p. 046314, 2011.

[7] W. Tang and S. G. Advani, "Drag on a nanotube in uniform liquid argon flow," *Journal of Chemical Physics*, vol. 125, p. 174706, 2006.

[8] K. Kordas, G. Toth, P. Moilanen, M. Kumpumaki, J. Vahakangas, A. Uusimaki, R. Vajtai, and P. M. Ajayan, "Chip cooling with integrated carbon nanotube microfin architectures," *Applied Physics Letters*, vol. 90, p. 123105, 2007.

[9] A. Pathak, J. AuBuchon, D. Brei, J. Shaw, J. Luntz, and S. Jin, "Carbon nanotube fins for the enhanced cooling of shape memory allow wire," *Behaviour and mechanics of multifunctional and composite materials*, vol. 6929, pp. 69 291K1–8, 2008.

[10] Y. Peles, A. Kosar, C. Mishra, C.-J. Kuo, and B. Schneider, "Forced convective heat transfer across a pin fin micro heat sink," *International Journal of Heat and Mass Transfer*, vol. 48, pp. 3615–3627, 2005.

[11] S. Sawano, T. Arie, and S. Akita, "Carbon nanotube resonator in liquid," *Nanoletters*, vol. 10, pp. 3395–3398, 2010.

[12] A. Eichler, J. Moser, J. Chaste, M. Zdrojek, I. Wilson-Rae, and A. Bachtold, "Nonlinear damping in mechanical resonators made from carbon nanotubes and graphene," *Nature Nanotechnology*, vol. 6, pp. 339–342, 2011.

[13] J. Chaste, A. Eichler, J. Moser, G. Ceballos, R. Rurali, and A. Bachtold, "A nanomechanical mass sensor with yoctogram resolution," *Nature Nanotechnology*, vol. Vol 7, pp. 301–304, 2012.

[14] H. Hosaka, Kiyoshi, Itao, and S. Kuroda, "Damping characteristics of beam-shaped micro-oscillators," *Sensors and Actuators A*, vol. 49, pp. 87–95, 1995.

[15] R. B. Bhiladvala and Z. J. Wang, "Effect of fluids on the Q factor and resonance frequency of oscillating micrometer and nanometer scale beams," *Physical Review E*, vol. 69, p. 036307, 2004.

[16] P. Dhiman, F. Yavari, X. Mi, H. Gullapalli, Y. Shi, P. M. Ajayan, and N. Koratkar, "Harvesting energy from water flow over graphene," *Nanoletters*, vol. 11, pp. 3123–3127, 2011.

[17] M. E. Tuckerman, *Statistical Mechanics: Theory and Molecular Simulation*. United States: Oxford University Press Inc., New York, 2010.

[18] S. Plimpton, "Fast parallel algorithms for short-range molecular dynamics," *J Comp. Phys.*, vol. 117, pp. 1–19, 1995.

[19] T. Werder, J. H. Walther, R. L. Jaffe, T. Halicioglu, F. Noca, and P. Koumoutsakos, "Molecular dynamics simulation of contact angles of water droplets in carbon nanotubes," *Nanoletters*, vol. 1, pp. 697–702, 2001.

[20] L. Verlet, "Computer "experiments" on classical fluids. I. thermodynamical properties of Lennard-Jones molecules," *Physical Review*, vol. 159, pp. 98–103, 1967.

[21] S. Nosé, "A unified formulation of the constant temperature molecular dynamics methods," *J. Chem. Phys.*, vol. 81, p. 511, 1984.

[22] M. E. Tuckerman, *Statistical Mechanics: Theory and molecular simulation*. United States of America: Oxford University Press, 2010, pp. 178–195.

[23] R. L. Rowley and M. M. Painter, "Diffusion and viscosity equations of state for a Lennard-Jones fluid obtained from molecular dynamics simulations," *International Journal of Thermophysics*, vol. 18, p. 1109, 1997.

[24] K. Meier, A. Laesecke, and S. Kabelac, "Transport coefficients of the Lennard-Jones model fluid. I. viscosity," *Journal of Chemical Physics*, vol. 121, p. 3671, 2001.

[25] H. J. C. Berendsen, J. R. Grigera, and T. P. Straatsma, "The missing term in effective pair potentials," *Journal of Physical Chemistry*, vol. 91, pp. 6269–6271, 1987.

[26] T. Werder, J. H. Walther, and P. Koumoutsakos, "Hybrid atomistic-continuum method for the simulation of dense fluid flows," *Journal of Computational Physics*, vol. 205, pp. 373–390, 2004.

[27] W. Shinoda, M. Shiga, and M. Mikami, "Rapid estimation of elastic constants by molecular dynamics simulation under constant stress," *Phys. Rev. B*, vol. 69, p. 134103, 2004.

[28] G. J. Martyna, D. J. Tobias, and M. L. Klein, "Constant pressure molecular dynamics algorithm," *J. Chem. Phys.*, vol. 101, p. 4177, 1994.

[29] M. Parrinello and A. Rahman, "Polymorphic transitions in single crystals: A new molecular dynamics method," *J. Appl. Phys.*, vol. 52, p. 7182, 1981.

[30] T. Werder, J. H. Walther, R. L. Jaffe, T. Halicioglu, and P. Koumoutsakos, "On the water-carbon interaction for use in molecular dynamics simulations of graphite and carbon nanotubes," *J Physical Chemistry B*, vol. 107, pp. 1345–1352, 2003.

[31] M. A. González and J. L. F. Abascal, "The shear viscosity of rigid water models," *J. Chem. Phys.*, vol. 132, p. 096101, 2010.

[32] H. Hasimoto, "On the periodic fundamental solutions of the Stokes equations and their application to viscous flow past a cubic array of spheres," *J. Fluid Mech.*, vol. 5, pp. 317–328, 1959.

[33] A. S. Sangani and A. Acrivos, "Slow flow through a periodic array of spheres," *International Journal of Multiphase Flow*, vol. 8, no. 4, pp. 343–360, 1982.

[34] D. L. Koch and A. J. C. Ladd, "Moderate Reynolds number flows through periodic and random arrays of aligned cylinders," *J. Fluid Mech.*, vol. 349, pp. 31–66, 1997.

[35] G. K. Batchelor, *An introduction to fluid dynamics*. United States of America: Cambridge University Press, 2000, pp. 227–228.

[36] K. Shintani, A. Umemura, and A. Takano, "Low-Reynolds-number flow past an elliptic cylinder," *J. Fluid Mech.*, vol. 136, pp. 277–289, 1983.

[37] S. K. Kannam, B. D. Todd, J. S. Hansen, and P. J. Daivis, "Slip flow in graphene nanochannels," *J. Chem. Phys.*, vol. 135, p. 144701, 2011.

[38] S. K. Kannam, B. D. Todd, J. S. Hansen, and P. J. Daivis, "Slip length of water on graphene: limitations of non-equilibrium molecular dynamics simulations," *J. Chem. Phys.*, vol. 136, p. 024705, 2012.

[39] S. K. Kannam, B. D. Todd, J. S. Hansen, and P. J. Daivis, "How fast does water flow in carbon nanotubes," *J. Chem. Phys.*, vol. 138, p. 094701, 2013.

[40] A. J. Chorin, "Numerical solution of the Navier-Stokes equations," *Mathematics of Computation*, vol. 22, pp. 745–762, 1968.

[41] K. Meier, "Computer simulation and interpretation of the transport coefficients of the Lennard-Jones model fluid," Dissertation, 2002.

[42] I. Bitsanis, J. J. Magda, M. Tirrell, and H. T. Davis, "Molecular dynamics of flow in micropores," *J. Chemical Physics*, vol. 87, no. 3, pp. 1733–1750, 1987.

[43] L. V. Woodcock, "Equation of state for the viscosity of Lennard-Jones fluids," *American Institute of Chemical Engineers*, vol. 52, no. 2, pp. 438–446, 2005.

[44] M. M. Papari, "Transport properties of carbon dioxide from an isotropic and effective pair potential energy," *Chemical Physics*, vol. 288, p. 249, 2002.

[45] G. K. Batchelor, *An introduction to fluid dynamics*. United States of America: Cambridge University Press, 2000.